Results in Chemistry 6 (2023) 101031

Contents lists available at ScienceDirect

Results in Chemistry

journal homepage: www.sciencedirect.com/journal/results-in-chemistry

Exploring the role of different morphologies of β–$Ni(OH)_2$ for electrocatalytic urea oxidation and the effects of electrochemically active surface area

Maryam Toufani [1], Hanka Besic [1], Wenming Tong [*], Pau Farràs [*]

School of Biological and Chemical Sciences and Energy Research Centre, Ryan Institute, University of Galway, University Road, H91 CF50 Galway, Ireland

ARTICLE INFO

Keywords:
Urea Oxidation Reaction
$Ni(OH)_2$
Electrocatalysis
Morphology
Active site

ABSTRACT

$Ni(OH)_2$, as a multifunctional material, has found its applications in a great number of research areas. In particular, it is an efficient catalyst for urea oxidation reaction (UOR), which is an important alternative to oxygen evolution reaction in electrocatalytic water splitting. This work investigates the effect of materials morphology on the electrocatalytic UOR performance of β–$Ni(OH)_2$, as well as the importance of characterising the catalysts' surface by electrochemical active surface area. Three different morphologies (nanoflowers, nanocubes, and nanosheets) were prepared via a simple hydrothermal approach. The morphology and structure of the as-prepared samples were carefully examined by scanning electron microscopy, transmission electron microscopy, and powder X-ray diffraction. The UOR performance of β–$Ni(OH)_2$ was evaluated by means of cyclic voltammetry, linear sweep voltammetry, Tafel analysis, and electrochemical surface area. Nanosheet $Ni(OH)_2$ electrocatalyst exhibits higher current density responses (28.3 mA $cm^{-2}{}_{ECSA}$ at 1.6 V vs. RHE) and a lower slope in the Tafel plot (72.6 mV dec^{-1}). Consequently, due to the exposure of more active sites to the reactants, the Ni $(OH)_2$ electrode with nanosheet morphology displayed higher electrocatalytic performance during UOR compared to the nanoflower and nanocube samples.

Introduction

Combining hydrogen production with oxidation reactions of favourable thermodynamics, such as urea, alcohol, and 5-hydroxymethylfurfural [1,2] oxidation in a water splitting process has attracted much attentions since the oxygen evolution half reaction (OER) is kinetically more challenging, and needs a large overpotential to drive the entire reaction [3–5]. Urea electrolysis can be an efficient anodic half reaction to replace the OER in a basic environment due to its low thermodynamic potential and ability to reduce pollution in urea-containing wastewater [6,7]. The urea electrolysis eq (1) in alkaline environment has a 6-electron transfer mechanism that occurs at the anode eq (2), while the HER reaction occurs at the cathode eq (3) [8,9].

$$CO(NH_2)_2(aq) + H_2O(l) \rightarrow N_2(g) + CO_2(g) + 3H_2(g) \qquad \textit{Total Reaction} \tag{1}$$

$$CO(NH_2)_2(aq) + 6OH^- \rightarrow N_2(g) + 5H_2O(l) + CO_2(g) + 6e^- \qquad \textit{Oxidation} \tag{2}$$

$$6H_2O(l) + 6e^- \rightarrow 6OH^- + 3H_2(g) \qquad \textit{Reduction} \tag{3}$$

The oxidation potential for UOR is 0.37 V vs RHE, which is significantly lower than that of OER (1.23 V) [10–12]. In addition, the UOR is an effective method for the treatment of urine-containing wastewater. Significant contributors to the generation of urea-containing wastewater are humans, animals, industry, and agricultural fertilizers. When ammonia decomposes in water wastes, it can be transformed to toxic nitrates, nitrites, and nitrogen oxides [13]. The use of urea as the anodic reaction can reduce the environmental pollution by increasing CO_2 and N_2 recycling [12,14]. Despite the aforementioned advantages, UOR's overall efficiency is rather low, and therefore, cheap and highly efficient catalysts are needed to improve the effectiveness of UOR. Among various transition metal derived catalysts, nickel-based materials such as nickel hydroxides are effective catalysts for achieving high UOR performance under alkaline conditions, with low overpotential, high

* Corresponding authors.
E-mail addresses: wenming.tong@universityofgalway.ie (W. Tong), pau.farras@universityofgalway.ie (P. Farràs).
[1] These authors equally contributed to this work.

https://doi.org/10.1016/j.rechem.2023.101031
Received 1 March 2023; Accepted 3 July 2023
Available online 5 July 2023

catalytic current, and durability [15–17]. The electrooxidation of urea on $Ni(OH)_2$ coated electrodes is shown in eqs (4) and (5). It consists of two steps: firstly, the $Ni(OH)_2$ is electrochemically oxidized to NiOOH at the anode, and this further oxidizes urea molecules to N_2 and CO_2 by a chemical pathway [1,18,19].

$$6Ni(OH)_2(s) + 6OH^- \rightleftharpoons 6NiOOH(s) + 6H_2O(l) + 6e^- \quad \textit{Electrochemical Oxidation} \tag{4}$$

$$6NiOOH(s) + CO(NH_2)_2(aq) + H_2O(l) \rightarrow 6Ni(OH)_2(s) + N_2(g) + CO_2(g) \quad \textit{Chemical Oxidation} \tag{5}$$

Nickel-based electrodes have been studied thoroughly for alkaline water electrolysis [20–22]. In terms of nickel hydroxide, two main crystalline phases exist, α–$Ni(OH)_2$ (rhombohedral) and β–$Ni(OH)_2$ (hexagonal) [23]. The α–$Ni(OH)_2$ has a larger space between interlayers (>7.5 Å) allowing for the presence of anions such as nitrate, carbonate, sulphate, and water molecules [24]. β–$Ni(OH)_2$, on the other hand, has a more organized structure with layers oriented along the c axis and a smaller interlayer space (4.60 Å) [25–27]. Among these two phases, β–$Ni(OH)_2$, demonstrates excellent chemical and thermal stability especially in alkaline media [28,29]. Prior investigations focused on the various morphologies of α–$Ni(OH)_2$ and β–$Ni(OH)_2$, as well as their performance in urea oxidation reaction. For example, the current density of irregularly shaped β–$Ni(OH)_2$ was reported to reach as high as 166.2 mA cm^{-2} at 1.6 V [30]. Due to Ni^{3+} active species and a significant mass transfer, $Ni(OH)_2$ nanomesh exhibited higher current density (408 mA mg^{-1}) and lower onset potential (1.35 V) [22].

$Ni(OH)_2$ of various morphologies often expose different crystal facets, which might possess significantly varied amounts of catalytically active sites [31]. The thermodynamic stability of those facets also vary, a prior computational studies have identified low index facets (0 0 1), (0 1 0) and (1 0 0) as the most stable for β–$Ni(OH)_2$ [24]. Considering electrocatalytic processes primarily occur on the catalysts' surfaces, it would be beneficial to understand the activity-morphology relationship of catalysts. In addition, due to the varied morphologies, size, and crystallinity, it is practical to profile the catalysts' surface at the electrodes using electrochemical active surface area (ECSA) rather than geometric area that was employed in the majority of the previous reports. This makes it complicated to evaluate and compare the reported results in the literature [32]. With this in mind, the present work aims to demonstrate the effect of three different morphologies of β–$Ni(OH)_2$ on their activities toward urea oxidation reaction (UOR).

Experimental section

Materials

Analytical grade nickel nitrate hexahydrate (Acros Organics), nickel sulphate hexahydrate (Acros Organics), urea (Fluorochem), ammonia (Sigma Aldrich), sodium hydroxide (Fisher Scientific) were used as received without further purifications. Deionised water was used in the synthesis of materials, and Mili-Q water was used in electrochemical measurements throughout the experiment.

Synthesis of β–Ni(OH)$_2$ nanoflower (β–Ni(OH)$_2$_NF)

1.40 g of $Ni(NO_3)_2{\cdot}6H_2O$, 0.29 g of $CO(NH_2)_2$, and 1.095 mL $NH_3{\cdot}H_2O$ (35%) were mixed with 80 mL deionised water and magnetically stirred for 15 min at 520 rpm. Solutions were transferred into a Teflon cup of 100 mL capacity in a stainless steel-lined autoclave. The autoclave was maintained at 100 °C for 2 h and then cooled to room temperature naturally. After the reaction, the green powder was washed with deionised water several times until the pH of the supernatant is equal to that of deionised water. Finally, ethanol was used to remove the residual water. The final product was obtained after drying at 80 °C for 12 h.

Synthesis of β–Ni(OH)$_2$ nanosheet (β–Ni(OH)$_2$_NS)

0.079 g of NaOH were dissolved in 10 mL deionised water and added slowly into the 0.1 M $NiSO_4{\cdot}6H_2O$ aqueous solution (10 mL) under vigorous stirring at 1300 rpm. The solution was stirred for 30 min and then transferred to a 100 mL Teflon-line autoclave. The autoclave was kept at 180 °C for 8 h, then allowed to cool down to room temperature. The product was separated by centrifugation at 5000 rpm for 10 min. Finally, the obtained product was washed with deionised water until the pH of the supernatant is the same as that of deionised water, and then ethanol to remove the remaining water. The final product was dried in an oven at 50 °C for 12 h.

Synthesis of β–Ni(OH)$_2$ nanocubes (β–Ni(OH)$_2$_NCs)

1.61 g of NaOH were dissolved in 20 mL deionised water and slowly added into the 1 M $NiSO_4{\cdot}6H_2O$ solution (20 mL) under vigorous stirring at 1300 rpm. The solution was stirred for 30 min and then transferred to a 100 mL Teflon-line autoclave. The autoclave was kept at 180 °C for 4 h, then allowed to cool down to room temperature. The product was separated by centrifugation at 5000 rpm for 10 min. The cleaning process was the same as for the β–$Ni(OH)_2$_NS sample.

Materials characterization

Powder X-ray diffraction (PXRD) data of β–$Ni(OH)_2$_NF was collected on a D8 advance series 2Theta/Theta powder diffractometer at room temperature and Phase analysis of β–$Ni(OH)_2$_NC and β–$Ni(OH)_2$_NS samples were performed by X-ray powder diffraction using an Intel Equinox 6000 system with a 1.54056 nm Cu α-1 X-ray source. Scanning electron microscopy (SEM) was used to observe the morphology and size of prepared samples. The SEM was performed on Hitachi SEM (S-4700), which was fitted with the Oxford Instruments INCA Energy EDX detector. For sample preparation, 2 mg samples were dispersed in 0.5 mL ethanol and sonicated for 2 h. Then 10 μL of the suspension were drop-casted onto a clean silicon wafer, which was then attached to a sample holder. Before SEM characterization, the samples were sputter-coated with a thin layer of gold. TEM measurements were carried out on a Hitachi H7500 electron microscope. All images were taken at 100 kV at room temperature. The TEM grids were prepared in the following steps: the samples were first dispersed in ethanol by sonication. A small volume of the suspensions was drop-casted on 200 mesh copper grids with Formvar/Carbon membrane coatings.

Electrochemical characterization

All electrochemical measurements were conducted using a PalmSens3 portable potentiostat and a Metrohm Multi Autolab M204 potentiostat in a conventional three-electrode system. Glassy carbon electrode coated with electrocatalysts, Pt wire, and saturated Hg/HgO were used as the working electrode, counter electrode, and reference electrode, respectively. All the potentials were converted to a reversible

hydrogen electrode (RHE) potential scale: $E_{RHE} = E_{Hg/HgO} + 0.591*pH + 0.098$.

The working electrodes were prepared by a drop–casting method. The catalyst inks were prepared by dispersing 16.0 mg of the catalyst and 4.0 mg of carbon black (Vulcan XC-72) in 1.0 mL of aqueous solution containing 750 μL of MiliQ water and 250 μL of ethanol. Then the ink was sonicated for 6 h to achieve good electrocatalyst dispersion. After the sonication, 100 μL of 5 wt% Nafion dispersion was added to the catalyst ink and further sonicated for 15 min. In the end, 3 μL of the resulting dispersion was deposited onto the surface of previously polished glassy carbon electrode (3 mm diameter, 0.071 cm^2) and allowed to dry under an IR lamp. The catalyst loading on the glassy carbon electrode was calculated to be 0.676 mg cm^{-2}. All electrochemical tests were conducted in 1 M KOH with and/or without 0.33 M urea at room temperature. Cyclic voltammetry (CV) were investigated under the potential window of 1.12–1.72 V (vs. RHE) and a scan rate of 50 mV s^{-1}. The electrochemical data are normalized with respective to the electrochemical surface area of the catalysts (see electrochemical oxidation of urea). The working-electrode geometrical areas were normalized in all the CVs and LSVs to obtain the current densities. The Tafel plots are obtained from forward-scan LSVs and the corresponding Tafel slopes were derived from the ECSA corrected polarization curves. The Tafel plot is fitted from the Tafel equation: $\eta = b \times \log j + a$, where η is overpotential, j is current density, b is Tafel slope, and a is Tafel constant. Electrochemical impedance spectroscopy (EIS) measurements were performed using an AC amplitude of 10 mV in the frequency range of 0.1 Hz and 100 kHz.

Chronopotentiometry was carried out in 0.33 M urea in 1.0 M KOH at 20 mA cm^{-2} to investigate the stability of the catalysts. Nickel foam was used as a substrate for all the stability tests. For the nickel foam (NF) preparation, the nickel foam substrate (1 cm^2) was first sonicated in 3 M HCl for 15 min, which is followed by sonication in acetone for 30 min and another sonication step in ethanol for 15 min. Finally, nickel foam was sonicated in deionised water for 30 min. After sonication steps, NF were dried for 10 min at 70 ℃ in the oven and under IR lamp for 5 min. The nickel foam electrodes were prepared by dip-coating method. Cleaned nickel foam was dipped into the catalyst ink solution for 30 s and then removed and dried under IR lamp for 5 min. Then these steps were repeated two more times. It is noted that the area of the nickel foam was 1 cm^2 for each sample and the catalyst loading on the glassy carbon electrode was calculated to be around 3.0 mg cm^{-2}.

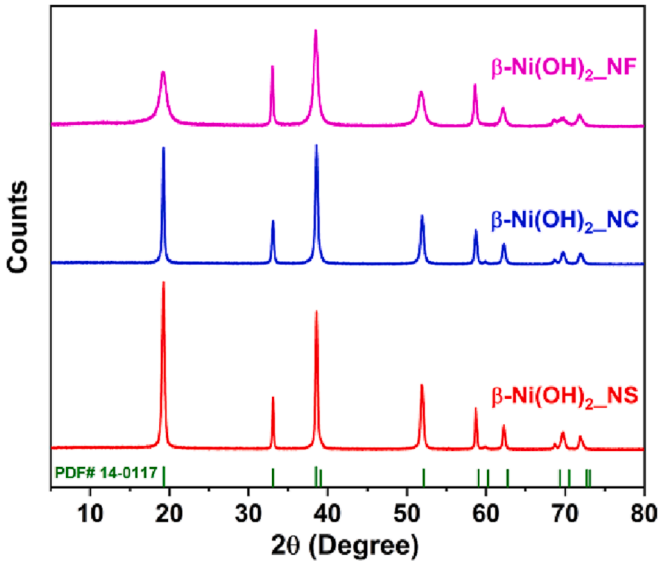

Fig. 1. PXRD Patterns of β–$Ni(OH)_2$_NF, β–$Ni(OH)_2$_NCs and β–$Ni(OH)_2$_NS. The vertical lines in olive represent the data from PDF card No. 14–0117 for β–$Ni(OH)_2$.

Results and discussion

The phase structure and purity of the β–$Ni(OH)_2$_NF, β–$Ni(OH)_2$_NCs and β–$Ni(OH)_2$_NS samples were examined by PXRD. The diffraction patterns in Fig. 1 support the formation of the β–phase $Ni(OH)_2$ (JCPDS No: 14–0117). The main diffraction peaks at 19.3°, 33.1°, 38.5°, 52°.03, 59.1°, 62.8°, 70.5°, 72.8° correspond to the (0 0 1), (1 0 0), (1 0 1), (1 0 2), (1 1 0), (1 1 1), (1 0 3), and (2 0 1) planes of β–$Ni(OH)_2$, respectively. Sharper reflection peaks on the β–$Ni(OH)_2$_NCs and β–$Ni(OH)_2$_NS samples indicate a greater degree of ordering and crystallinity due to the higher synthetic temperatures. No peaks related to other impurities were observed, which indicates well-defined crystalline structure, and good sample purity.

SEM and TEM were used to examine the morphologies of the synthesised products. Low magnification SEM images in Fig. 2a-c demonstrate that all three samples were composed of rather uniform and homogeneously distributed particles. It is shown that $Ni(OH)_2$_NF, as seen in Fig. 2d, is made of flower-like structures of assembled plates with an average size of 1.0 μm. Fig. 2e and 2f show SEM images of β–$Ni(OH)_2$_NC and β–$Ni(OH)_2$_NS samples at higher magnifications, synthesized at different time scales by the hydrothermal method. β–$Ni(OH)_2$_NC has a cube shape with an average size of 58 nm, while β–$Ni(OH)_2$–NS, which was synthesized over a longer period of time, has an homogenous hexagonal sheet structure with an average size around 190 nm. The TEM images shown in Fig. 3a-c exhibit a more detailed morphology of the samples, providing additional evidence for their floral, cube and sheet structures.

Electrochemical oxidation of urea

The electrochemical measurements of the prepared nickel hydroxide with different morphologies were studied using a three-electrode system. Cyclic voltammetry (CV) measurements were carried out in 1 M KOH with and without the presence of urea at the scan rate of 50 mV s^{-1}. To normalize the current density based on an appropriate parameter, the electrochemical double-layer capacitance (C_{dl}) approach was used to estimate the electrochemically active surface area (ECSA) from cyclic voltammetry curves in a non-Faradaic region at various scan rates (25, 75, 100 and 125 mV s^{-1}). The potential window between 0.82 and 1.02 V was used for the ECSA measurement. The double-layer capacitance was obtained by plotting the $\Delta j = (j_a - j_c)$ at 0.92 V vs RHE as a function of the scan rate. The ECSA of the electrocatalysts was determined based on the following equation: $ECSA = C_{dl}/C_s$ where C_s represents the specific capacitance of a flat electrode, reported as 0.04 mF cm^{-2} for nickel hydroxide in alkaline solution [33]. Then, the slope was calculated to get the C_{dl} value, which is directly proportional to ECSA. The results are shown in Fig. S1, S2, and Table 1. C_{dl} value for nanocubes is in good agreement with the literature values of 0.14 mF cm^{-2} [34].

Both C_{dl} and ECSA have been employed to normalize the current densities in literature [35,36]. Here, ECSA is used to normalize the current responses of the synthesized electrocatalysts. As observed in Fig. S3, the ECSA-normalized current density of β–$Ni(OH)_2$ nanosheets is the largest amongst the three samples, indicating that the nanosheet morphology has more exposed Ni^{2+} active sites. On the other hand, nanocubes showcase a rather low current density, which is unexpected as β−$Ni(OH)_2$ nanocubes recorded the highest ECSA amongst the three morphologies. This suggests that ECSA and the numbers of OER active sites are not directly related in the case of β−$Ni(OH)_2$ nanocubes, that the active sites are not as accessible as for the other two morphologies. The three cyclic voltammograms shown in Fig. 4 illustrate typical redox characteristics of Ni-based electrocatalysts. Two peaks can be observed for the synthesised electrocatalysts. In the anodic scan, the peak at 1.5 V corresponds to the oxidation of Ni^{2+} ($Ni(OH)_2$) to Ni^{3+} (NiOOH), while the reverse cathodic peak at 1.2 V, corresponds to the reduction of Ni^{3+} to Ni^{2+} [37]. For β−$Ni(OH)_2$ nanocubes, the peak in the anodic scan was shifted to a slightly higher potential value compared to β−$Ni(OH)_2$

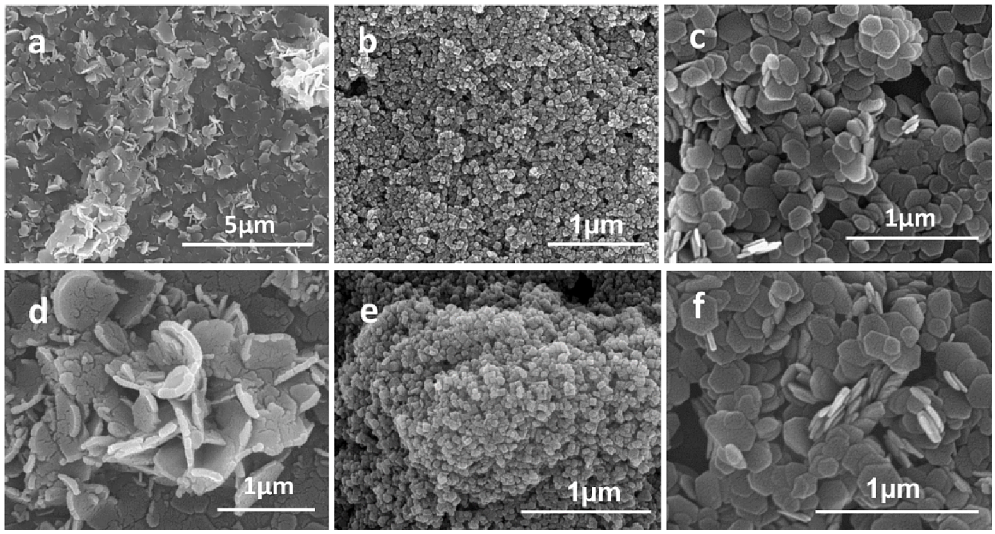

Fig. 2. SEM of β–Ni(OH)$_2$ nanostructures (a) NF (b) NC and (c) NS obtained at low magnification and high magnification (d-f), respectively.

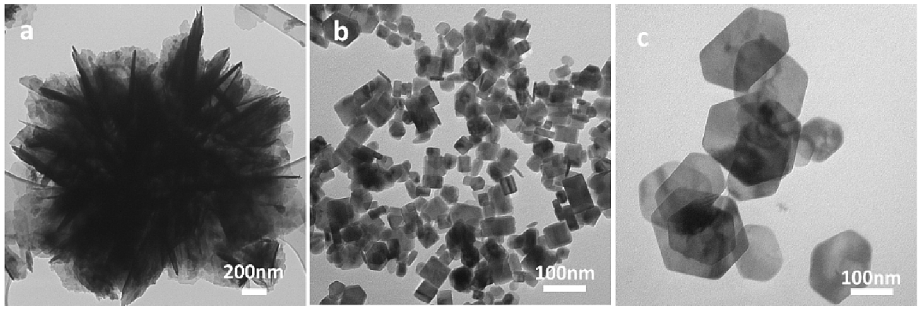

Fig. 3. TEM of β–Ni(OH)$_2$ nanostructures (a) NF (b) NC and (c) NS.

Table 1
Summary of electrochemical parameters for the synthesized electrocatalysts evaluated in 1 M KOH and 1 M KOH + 0.33 M urea. The double layer capacitance, electrochemically active surface area (ECSA) and Tafel slope were assessed.

Catalyst	C_{dl} (mF cm^{-2})	ECSA (cm^2)	Current Density at 1.6 V for UOR (mA $cm^{-2})_{ECSA}$	Tafel slope OER (mV dec^{-1})	Tafel slope UOR (mV dec^{-1})
β−Ni(OH)$_2$ nanoflowers	0.0098	0.245	20.6	309.7	94.7
β−Ni(OH)$_2$ nanosheets	0.0127	0.316	28.3	212.4	72.6
β−Ni(OH)$_2$ nanocubes	0.1311	3.278	2.7	295.9	98.8

nanosheets and nanoflowers. On the other hand, the peak for β−Ni(OH)$_2$ nanocubes and nanosheets in the cathodic scan is shifted to lower potentials at 1.18 V and 1.15 V, respectively. The differences in ΔE between morphologies are indicative of the accessibility to the active sites by the reagents.

The UOR performances of nickel hydroxide catalysts were evaluated in 1 M KOH with 0.33 M urea following literature methodologies. Fig. 5 shows the increased current density in the presence of urea in all the synthesised β−Ni(OH)$_2$ electrocatalysts, indicative of the occurrence of a new electrocatalytic process. The sharp increase in the anodic current is due to oxidation of urea, which coincides with the oxidation of Ni^{2+} to Ni^{3+}, leading to the formation of NiOOH active sites for UOR. In terms of the reduction process, there is a decrease in intensity of the reduction peak in the presence of urea, due to the consumption of NiOOH during the chemical reduction process occurring during the second step of urea oxidation eq (5).

Furthermore, Fig. 5 shows the linear sweep voltammetry curves of the different samples to compare the performance in the presence or absence of 0.33 M urea. The collected LSVs show the anodic oxidation peaks indicating the conversion of β–Ni(OH)$_2$ to β–NiOOH in the absence of urea, and the almost negligible electrocatalytic peak for OER at higher overpotentials. As expected, the addition of urea distinctly increases the current density in all samples indicating an electrocatalytic response to UOR. Compared to β–Ni(OH)$_2$ nanosheets and nanoflowers, which display higher activity for UOR, the catalytic current response of β–Ni(OH)$_2$ nanocubes is significantly lower under the same applied potential as it is shown in Fig. S4, suggesting that β−Ni(OH)$_2$ nanocubes requires significantly higher overpotentials due to lack of accessible active sites. The results normalized based on Cdl are also given in Fig. S5 for reference where the same results can be drawn. It is important to remember here that all samples have the same crystal phase and the main difference is the exposed crystalline facets as a consequence of different morphologies. As shown in Fig. 5d and Table 1, β−Ni(OH)$_2$ nanosheets exhibits a higher current density of 3.5 mA cm^{-2}_{ECSA} at 1.40 V, compared to 3.5 mA cm^{-2}_{ECSA} at 1.71 V of β−Ni(OH)$_2$ nanocubes. The drastic variations in the current densities (based on ECSA) of cubes, sheets, and flowers are highly likely due to the different morphologies that expose distinct crystal planes. Moreover, the crystal planes of β−Ni(OH)$_2$ contain different density levels of exposed Ni^{2+}, which is an integral part of the urea oxidation mechanism [38]. This deserves a dedicated study in the future.

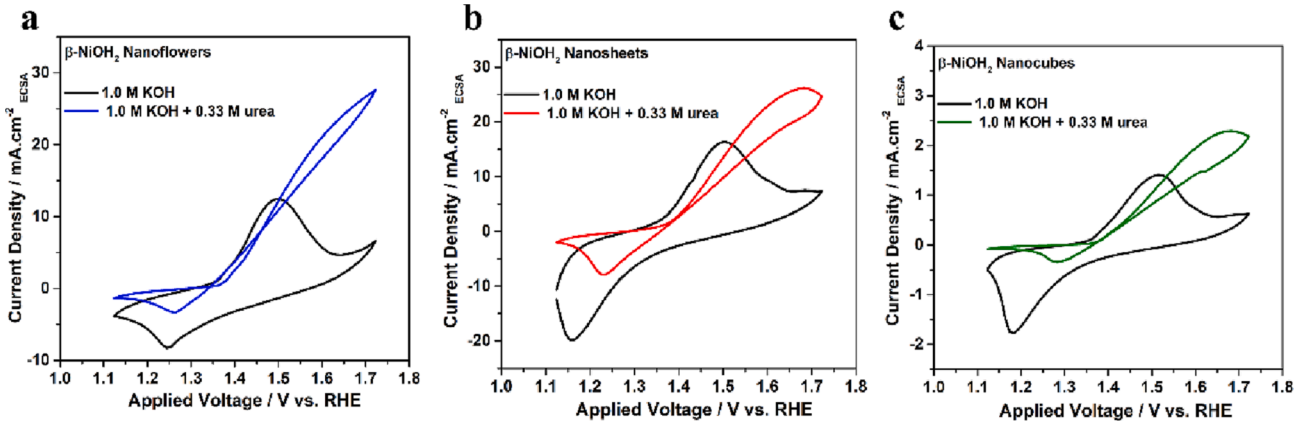

Fig. 4. Cyclic voltammograms of (a) β–$Ni(OH)_2$ nanoflowers; (b) β–$Ni(OH)_2$ nanosheets and (c) β–$Ni(OH)_2$ nanocubes in 1 M KOH and in the presence of 0.33 M urea at a scan rate of 50 mV s^{-1}. The potential axis is converted to reversible hydrogen electrode.

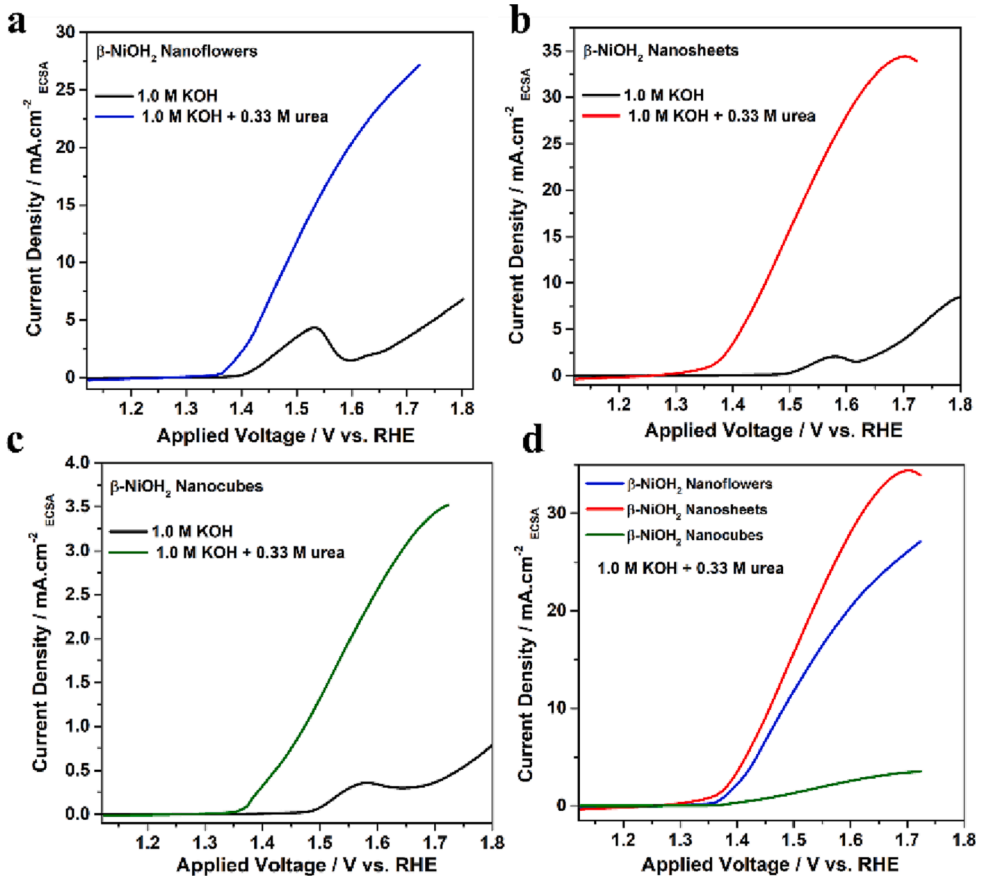

Fig. 5. Linear sweep voltammograms of (a) β−$Ni(OH)_2$ nanoflowers; (b) β−$Ni(OH)_2$ nanosheets, and (c) β−$Ni(OH)_2$ nanocubes in 1 M KOH and in the presence of 0.33 M urea. (d) Integrated LSV plots of UOR performance are given for direct comparison.

In addition, Tafel slopes were calculated to study the reaction kinetics under OER and UOR conditions. β−$Ni(OH)_2$ nanosheets possess the lowest Tafel slope of 212.4 mV dec^{-1} among the three catalysts for OER activities (Fig. 6a). The values were higher for β−$Ni(OH)_2$ nanoflowers (309.7 mV dec^{-1}) and β−$Ni(OH)_2$ nanocubes (295.9 mV dec^{-1}). In terms of the slopes obtained in the presence of urea (Fig. 6b, Table 1), all three morphologies feature much smaller values when compared to OER, which is expected, considering that UOR is a less demanding reaction and, therefore, the kinetic rates are larger. In addition, the same trend as in OER is observed where the fastest kinetics for UOR, corresponding to the smallest Tafel slope, are found for the β−$Ni(OH)_2$ nanosheet morphology, with a slope of 72.6 mV dec^{-1}.

When comparing this result with the ECSA normalized current density for UOR, Fig. S4 shows that the overpotential required for UOR is quite similar for nanoflower and nanosheet morphologies. Moreover, when comparing the slopes between nanosheet and nanoflowers (72.6 vs 94.7 mV dec^{-1}), we can conclude that the nanosheets have a higher intrinsic UOR catalytic activity.

To further investigate the electrocatalytic UOR kinetics of nickel hydroxide, we carried out electrochemical impedance spectroscopy (EIS) measurements at a constant potential of 1.40 V, corresponding to an overpotential $>$ 150 mV as suggested in the literature [36]. An

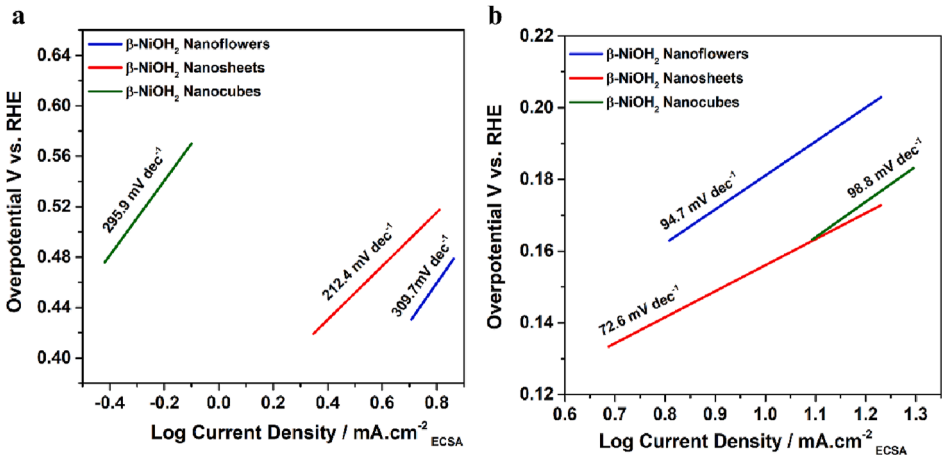

Fig. 6. (a) Tafel plots of β−Ni(OH)$_2$ nanosheets, nanoflowers and nanocubes in 1 M KOH; (b) Tafel plots of β−Ni(OH)$_2$ nanosheets, nanoflowers and nanocubes in 1 M KOH with 0.33 M urea.

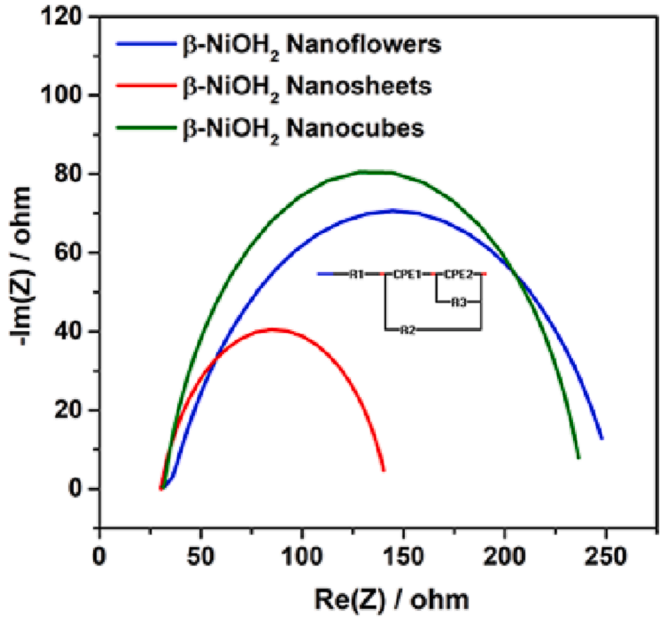

Fig. 7. Nyquist Plot of β−Ni(OH)$_2$ nanosheets, nanoflowers and nanocubes in 1 M KOH with 0.33 M urea; inset of schematic representation of the electrical circuit using the frequency range of 0.1 Hz to 100 kHz and 0.33 M urea at 1.4 V vs RHE.

equivalent circuit (shown in the inset of Fig. 7) for modelling the Faradaic impedance for urea electro-oxidation was used to extract the kinetic parameters of the catalysts in UOR. The impedance spectrum is fitted to the best-fitting equivalent circuit (R_1, R_2/CPE_1, R_3/CPE_2) previously reported for urea oxidation [39–41]. The parameters of circuits, which were extracted via EIS spectrum analyzer [42], were given in Table S2. The best-fitting equivalent circuit describes two charge transfer processes in addition to solution resistance, including the formation of NiOOH and urea degradation, as shown previously in eq (4) and (5). In this electrical circuit, R_1 (Rs) indicated the resistance of the solution between working electrode and reference electrode. The first charge transfer mechanism with R_2/CPE_1 is related to the electrochemical formation of NiOOH, whereas R_3/CPE_2 is related to the chemical oxidation of urea. Based on the fitted data (Table S2), R_3 values are much smaller compared to R_2 for all the morphologies. This shows that the electrochemical formation of Ni^{3+} active sites is predominant in each case. When comparing the different morphologies, nanosheets have a significantly smaller charge transfer resistance R_2/CPE_1 - compared to the other two morphologies (cubes and flowers) at 121, 208, and 222 Ω, respectively. Using the Nyquist ($Z^{/}$, -$Z^{//}$) plots as shown is Fig. 7, it is clear that β−Ni(OH)$_2$ nanosheets exhibits smaller diameter of the semicircle, attributed to lower faradaic impedance in the catalyst.

To further provide evidence for different activity relative to the specific morphology, the electrochemical stability was investigated by chronopotentiometry under a constant current density of 20 mA cm^{-2} in 1 M KOH and 0.33 M urea. It is important to note that the current density corresponds to the geometric area and not the ECSA normalized current, therefore it is expected that similar potentials are obtained (see Fig. S4). Fig S6 provides a direct comparison where only a negligible change is observed during a period of 8 h, suggesting the good stability of both β−Ni(OH)$_2$ nanosheets and β−Ni(OH)$_2$ nanocubes. As for the β−Ni(OH)$_2$ nanoflowers, the potential gradually increases with spikes appearing after ca. 4 h due to the disintegration of nanoflower morphology [39].

Conclusion

In this work, β−Ni(OH)$_2$ electrocatalysts featuring nanoflower, nanosheet, and nanocube morphologies were synthesized by a hydrothermal approach using different synthetic parameters and reaction times. The size and morphology of the synthesized catalysts were investigated by SEM and TEM, and the results confirmed the formation of nanoparticles with the targeted morphologies, with different shapes and sizes. The ECSA normalized current density show similar results for nanosheet and nanoflower, and a clear reduction in activity for the nanocubes, which is drastically different from the results obtained by geometric area. This shows the importance of using ECSA as surface area for comparison. The nanosheets morphology of β−Ni(OH)$_2$ expose far more active sites than the other morphologies, leading to better UOR activity in the presence of urea. EIS results further demonstrate that nanosheets have the least charge transfer resistance, while nanoflowers and nanocubes show similar values. Overall, the electrochemical results prove that electrocatalyst morphology has a significant effect on the catalytic activity in β−Ni(OH)$_2$ and this has direct implications on the preparation of nanostructured electrocatalysts for urea oxidation, as well as for water oxidation. Only by combining the results of ECSA-normalised current density, tafel plots and EIS, relevant conclusions on structure–activity relationship can be drawn. The electrocatalytic activity of β−Ni(OH)$_2$ for UOR can be significantly improved by chemical modification of the catalysts, but attention to different morphologies needs to be investigated to ensure optimum intrinsic activity and number of exposed active sites for catalysis. UOR represents a good

alternative to OER as a source of electrons for the production of green hydrogen, while also being a good anodic reaction in urea-rich wastewater sources.

CRediT authorship contribution statement

Maryam Toufani: Writing – review & editing. **Hanka Besic:** Writing – review & editing. **Wenming Tong:** Conceptualization, Supervision, Writing – review & editing. **Pau Farràs:** Conceptualization, Writing – review & editing, Supervision.

Declaration of Competing Interest

The authors declare that they have no known competing financial interests or personal relationships that could have appeared to influence the work reported in this paper.

Data availability

Data will be made available on request.

Acknowledgements

This work was funded by European Union's Horizon 2020 projects SOLAR2CHEM (Marie Skłodowska-Curie Actions with Grant Agreement No. 861151) and European Union Horizon 2020 - FlowPhotoChem project (Grant agreement number 862453). The authors acknowledge the scientific and technical assistance of Dr. Éadaoin Timmins in the use of the SEM and TEM within the Centre for Microscopy & Imaging funded by University of Galway and the Irish Government's Programme for Research in Third Level Institutions, Cycles 4 and 5, National Development Plan 2007–2013.

Appendix A. Supplementary data

Supplementary data to this article can be found online at https://doi.org/10.1016/j.rechem.2023.101031.

References

[1] J. Ge, Y. Lai, M. Guan, Y. Xiao, J. Kuang, C. Yang, Nickel borate with a 3D hierarchical structure as a robust and efficient electrocatalyst for urea oxidation, Environ. Sci Nano. 8 (2021) 1326–1335, https://doi.org/10.1039/d0en01247e.
[2] L. Wang, Y. Zhu, Y. Wen, S. Li, C. Cui, F. Ni, Y. Liu, H. Lin, Y. Li, H. Peng, B. Zhang, Regulating the Local Charge Distribution of Ni Active Sites for the Urea Oxidation Reaction, Angew Chemie. 133 (2021) 10671–10676, https://doi.org/10.1002/ange.202100610.
[3] X. Yang, L. Kang, Z. Wei, S. Lou, F. Lei, P. Hao, J. Xie, B. Tang, A self-sacrificial templated route to fabricate CuFe Prussian blue analogue/Cu(OH)2 nanoarray as an efficient pre-catalyst for ultrastable bifunctional electro-oxidation, Chem. Eng. J. 422 (2021), 130139, https://doi.org/10.1016/j.cej.2021.130139.
[4] Y. Liu, D. Zhou, T. Deng, G. He, A. Chen, X. Sun, Y. Yang, P. Miao, Research Progress of Oxygen Evolution Reaction Catalysts for Electrochemical Water Splitting, ChemSusChem. 14 (2021) 5359–5383, https://doi.org/10.1002/cssc.202101898.
[5] J. Ding, Z. Mo, X. Zhu, R. Yue, W. Liu, H. Pei, S. He, J. Zhu, H. Zheng, N. Liu, Co-Mof-Derived Zif@Ni-Co-B150 as an Efficient Electrocatalyst for Oxygen Evolution Reaction, SSRN Electron. J. (2022), https://doi.org/10.2139/ssrn.4111977.
[6] J. Xie, L. Gao, S. Cao, W. Liu, F. Lei, P. Hao, X. Xia, B. Tang, Copper-incorporated hierarchical wire-on-sheet α-Ni(OH)2 nanoarrays as robust trifunctional catalysts for synergistic hydrogen generation and urea oxidation, J. Mater. Chem. A. 7 (2019) 13577–13584, https://doi.org/10.1039/c9ta02891a.
[7] D. Zhu, H. Zhang, J. Miao, F. Hu, L. Wang, Y. Tang, M. Qiao, C. Guo, Strategies for designing more efficient electrocatalysts towards the urea oxidation reaction, J. Mater. Chem. A. 10 (2022) 3296–3313, https://doi.org/10.1039/d1ta09989b.
[8] J. Xie, H. Qu, F. Lei, X. Peng, W. Liu, L. Gao, P. Hao, G. Cui, B. Tang, Partially amorphous nickel-iron layered double hydroxide nanosheet arrays for robust bifunctional electrocatalysis, J. Mater. Chem. A. 6 (2018) 16121–16129, https://doi.org/10.1039/c8ta05054f.
[9] W. Sun, J. Li, W. Gao, L. Kang, F. Lei, J. Xie, Recent advances in the pre-oxidation process in electrocatalytic urea oxidation reactions, Chem. Commun. 58 (2022) 2430–2442, https://doi.org/10.1039/d1cc06290e.
[10] M. Hao, J. Chen, J. Chen, K. Wang, J. Wang, F. Lei, P. Hao, X. Sun, J. Xie, B. Tang, Lattice-disordered high-entropy metal hydroxide nanosheets as efficient precatalysts for bifunctional electro-oxidation, J. Colloid Interface Sci. 642 (2023) 41–52, https://doi.org/10.1016/j.jcis.2023.03.152.
[11] Y. Ren, C. Wang, W. Duan, L. Zhou, X. Pang, D. Wang, Y. Zhen, C. Yang, Z. Gao, Journal of Colloid and Interface Science MoS 2 / Ni 3 S 2 Schottky heterojunction regulating local charge distribution for efficient urea oxidation and hydrogen evolution, J. Colloid Interface Sci. 628 (2022) 446–455, https://doi.org/10.1016/j.jcis.2022.08.055.
[12] S.J. Patil, N.R. Chodankar, S.-K. Hwang, G.S. Rama Raju, Y.-S. Huh, Y.-K. Han, Fluorine Engineered Self-Supported Ultrathin 2D Nickel Hydroxide Nanosheets as Highly Robust and Stable Bifunctional Electrocatalysts for Oxygen Evolution and Urea Oxidation Reactions, Small. 18 (7) (2022) 2103326.
[13] Y. Ma, C. Ma, Y. Wang, K.e. Wang, Advanced Nickel-Based Catalysts for Urea Oxidation Reaction: Challenges and Developments, Catalysts. 12 (3) (2022) 337.
[14] P. Hao, W. Zhu, F. Lei, X. Ma, J. Xie, H. Tan, L. Li, H. Liu, B. Tang, Morphology and electronic structure modulation induced by fluorine doping in nickel-based heterostructures for robust bifunctional electrocatalysis, Nanoscale. 10 (2018) 20384–20392, https://doi.org/10.1039/c8nr06756b.
[15] J. Xie, W. Liu, X. Zhang, Y. Guo, L. Gao, F. Lei, B. Tang, Y. Xie, Constructing Hierarchical Wire-on-Sheet Nanoarrays in Phase-Regulated Cerium-Doped Nickel Hydroxide for Promoted Urea Electro-oxidation, ACS Mater. Lett. 1 (2019) 103–110, https://doi.org/10.1021/acsmaterialslett.9b00124.
[16] A.V. Munde, B.B. Mulik, P.P. Chavan, B.R. Sathe, Enhanced electrocatalytic activity towards urea oxidation on Ni nanoparticle decorated graphene oxide nanocomposite, Electrochim. Acta. 349 (2020), 136386, https://doi.org/10.1016/j.electacta.2020.136386.
[17] X. Jia, H. Kang, X. Yang, Y. Li, K. Cui, X. Wu, W. Qin, G. Wu, Amorphous Ni(III)-based sulfides as bifunctional water and urea oxidation anode electrocatalysts for hydrogen generation from urea-containing water, Appl. Catal. B Environ. 312 (2022), 121389, https://doi.org/10.1016/j.apcatb.2022.121389.
[18] J. Xie, W. Liu, F. Lei, X. Zhang, H. Qu, L. Gao, P. Hao, B. Tang, Y. Xie, Iron-Incorporated α-Ni(OH)2 Hierarchical Nanosheet Arrays for Electrocatalytic Urea Oxidation, Chem. - A Eur. J. 24 (2018) 18408–18412, https://doi.org/10.1002/chem.201803718.
[19] R.L. King, G.G. Botte, Investigation of multi-metal catalysts for stable hydrogen production via urea electrolysis, J. Power Sources. 196 (2011) 9579–9584, https://doi.org/10.1016/j.jpowsour.2011.06.079.
[20] Z. Wei, W. Sun, S. Liu, J. Qi, L. Kang, J. Li, S. Lou, J. Xie, B. Tang, Y. Xie, Lanthanum-doped α-Ni(OH)2 1D–2D-3D hierarchical nanostructures for robust bifunctional electro-oxidation, Particuology. 57 (2021) 104–111, https://doi.org/10.1016/j.partic.2021.01.002.
[21] K. Ye, H. Zhang, L. Zhao, X. Huang, K. Cheng, G. Wang, D. Cao, Facile preparation of three-dimensional Ni(OH)2/Ni foam anode with low cost and its application in a direct urea fuel cell, New J. Chem. 40 (2016) 8673–8680, https://doi.org/10.1039/c6nj01648k.
[22] Y. Ding, Y. Li, Y. Xue, B. Miao, S. Li, Y. Jiang, X. Liu, Y. Chen, Atomically thick Ni (OH) 2 nanomeshes for urea electrooxidation, Nanoscale. 11 (2019) 1058–1064, https://doi.org/10.1039/c8nr08104b.
[23] H. Dittrich, P. Axmann, M. Wohlfahrt-Mehrens, J. Garche, S. Albrecht, J. Meese-Marktscheffel, A. Olbrich, G. Gille, Structural study β-Ni(OH)2 and α-Ni(OH)2 variants for electrode applications, Zeitschrift Fur Krist. 220 (2005) 306–315, https://doi.org/10.1524/zkri.220.2.306.59135.
[24] A.J. Tkalych, K. Yu, E.A. Carter, Structural and Electronic Features of β-Ni(OH)2 and β-NiOOH from First Principles, J. Phys. Chem. C. 119 (2015) 24315–24322, https://doi.org/10.1021/acs.jpcc.5b08481.
[25] M. Aghazadeh, M. Ghaemi, B. Sabour, S. Dalvand, Electrochemical preparation of α-Ni(OH)2 ultrafine nanoparticles for high-performance supercapacitors, J. Solid State Electrochem. 18 (2014) 1569–1584, https://doi.org/10.1007/s10008-014-2381-7.
[26] M. Wehrens-Dijksma, P.H.L. Notten, Electrochemical Quartz Microbalance characterization of Ni(OH)2-based thin film electrodes, Electrochim. Acta. 51 (2006) 3609–3621, https://doi.org/10.1016/j.electacta.2005.10.022.
[27] S. Krehula, M. Ristić, C. Wu, X. Li, L. Jiang, J. Wang, G. Sun, T. Zhang, M. Perović, M. Bošković, B. Antić, L.K. Krehula, B. Kobzi, S. Kubuki, S. Musić, Influence of Fe (III) doping on the crystal structure and properties of hydrothermally prepared β-Ni (OH)2 nanostructures, J. Alloys Compd. 750 (2018) 687–695, https://doi.org/10.1016/j.jallcom.2018.04.032.
[28] Y. Wang, X. Luo, W. Lu, B. Huang, Y. Yang, Fabrication of Flower-like Rhodium-Doped β-Ni(OH)2as an Efficient Electrocatalyst for Methanol Oxidation Reaction in Alkaline Media, Langmuir. 39 (1) (2023) 423–432.
[29] G.X. Tong, F.T. Liu, W.H. Wu, J.P. Shen, X. Hu, Y. Liang, Polymorphous α- And β-Ni (OH) 2 complex architectures: Morphological and phasal evolution mechanisms and enhanced catalytic activity as non-enzymatic glucose sensors, CrystEngComm. 14 (2012) 5963–5973, https://doi.org/10.1039/c2ce25622c.
[30] Q. Cao, Y. Yuan, K. Wang, W. Huang, Y. Zhao, X. Sun, R. Ding, W. Lin, E. Liu, P. Gao, Phase and crystallinity regulations of Ni(OH)2 by vanadium doping boost electrocatalytic urea oxidation reaction, J. Colloid Interface Sci. 618 (2022) 411–418, https://doi.org/10.1016/j.jcis.2022.03.054.
[31] T. Chen, Y. Bai, X. Xiao, H. Pang, Exposing (0 0 1) crystal facet on the single crystalline β-Ni(OH)2 quasi-nanocubes for aqueous Ni-Zn batteries, Chem. Eng. J. 413 (2021), 127523, https://doi.org/10.1016/j.cej.2020.127523.
[32] S. Sun, H. Li, Z.J. Xu, Impact of Surface Area in Evaluation of Catalyst Activity, Joule. 2 (2018) 1024–1027, https://doi.org/10.1016/j.joule.2018.05.003.
[33] C.C.L. McCrory, S. Jung, J.C. Peters, T.F. Jaramillo, Benchmarking heterogeneous electrocatalysts for the oxygen evolution reaction, J. Am. Chem. Soc. 135 (2013) 16977–16987, https://doi.org/10.1021/ja407115p.

[34] L. Yang, B. Zhang, W. Ma, Y. Du, X. Han, P. Xu, Pearson's principle-inspired strategy for the synthesis of amorphous transition metal hydroxide hollow nanocubes for electrocatalytic oxygen evolution, Mater. Chem. Front. 2 (2018) 1523–1528, https://doi.org/10.1039/c8qm00170g.
[35] J. Xie, S. Li, X. Zhang, J. Zhang, R. Wang, H. Zhang, B. Pan, Y. Xie, Atomically-thin molybdenum nitride nanosheets with exposed active surface sites for efficient hydrogen evolution, Chem. Sci. 5 (2014) 4615–4620, https://doi.org/10.1039/c4sc02019g.
[36] S. Anantharaj, S. Kundu, Do the Evaluation Parameters Reflect Intrinsic Activity of Electrocatalysts in Electrochemical Water Splitting? ACS Energy Lett. 4 (2019) 1260–1264, https://doi.org/10.1021/acsenergylett.9b00686.
[37] R.K. Singh, A. Schechter, Electrochemical investigation of urea oxidation reaction on β Ni(OH)2 and Ni/Ni(OH)2, Electrochim. Acta. 278 (2018) 405–411, https://doi.org/10.1016/j.electacta.2018.05.049.
[38] B. Lv, Z. Liu, R. Ding, D. Wu, Y. Xu, Fast production of β-Ni(OH)2 nanostructures with (001) and (100) plane exposure and their electrochemical properties, J. Mater. Chem. A. 1 (2013) 5695–5699, https://doi.org/10.1039/c3ta10375g.
[39] T.H. Wu, B.W. Hou, Superior catalytic activity of α-Ni(OH)2for urea electrolysis, Catal, Sci. Technol. 11 (2021) 4294–4300, https://doi.org/10.1039/d1cy00435b.
[40] I.M.A. Mohamed, P. Kanagaraj, A.S. Yasin, W. Iqbal, C. Liu, Electrochemical impedance investigation of urea oxidation in alkaline media based on electrospun nanofibers towards the technology of direct-urea fuel cells, J. Alloys Compd. 816 (2020), 152513, https://doi.org/10.1016/j.jallcom.2019.152513.
[41] I.M.A. Mohamed, C. Liu, Chemical design of novel electrospun CoNi/Cr nanoparticles encapsulated in C-nanofibers as highly efficient material for urea oxidation in alkaline media, Appl. Surf. Sci. 475 (2019) 532–541, https://doi.org/10.1016/j.apsusc.2019.01.003.
[42] R.G.A. Bondarenko A. S., In Progress in Chemometrics Research, Pomerantsev A. L., Ed.; Nova Science Publishers:, (n.d.). http://www.abc.chemistry.bsu.by/vi/analyser/program/program.htm.